International Journal of Heat and Mass Transfer 51 (2008) 5052–5062

Contents lists available at ScienceDirect

International Journal of Heat and Mass Transfer

journal homepage: www.elsevier.com/locate/ijhmt

Simulations of a prototypical device using pyroelectric materials for harvesting waste heat

Damien Vanderpool, Jeong Hwan Yoon, Laurent Pilon *

University of California, Los Angeles, Henry Samueli School of Engineering and Applied Science, Mechanical and Aerospace Engineering Department, 420 Westwood Plaza, Eng. IV 37-132, Los Angeles, CA 90095-1597, USA

ARTICLE INFO

Article history:
Received 3 January 2008
Received in revised form 3 April 2008
Available online 26 June 2008

Keywords:
Pyroelectric
Direct energy conversion
Waste heat
Optimum efficiency
Power density
Numerical simulation

ABSTRACT

This paper is concerned with directly converting waste heat into electricity using pyroelectric materials. A prototypical pyroelectric converter is simulated by solving the two-dimensional mass, momentum, and energy equations using finite element methods. The pumping power and the electrical power generated are estimated from the computed pressure, temperature, and velocity. The results show that the energy efficiency increases as the density and specific heat of the working fluid and of the pyroelectric material decrease. Moreover, the power density increases as the density and specific heat of the working fluid increase and those of the pyroelectric material decrease. One can reasonably achieve an energy efficiency of 40% of the Carnot efficiency and a power density of 24 W/L of pyroelectric materials.

1. Introduction

Recently, direct energy-conversion devices have received significant attention due to the necessity to develop cleaner and more efficient ways of transforming available forms of primary energy into electrical power. For example, thermoelectric generators based on the Seebeck effect result in the creation of an electromagnetic force in the presence of a steady-state temperature difference between two junctions of different semiconductors. However, heat diffusion may occur between the hot and the cold sources and negatively affect the performances. Commercial thermoelectric generators have efficiencies that are "typically around 5%" [1].

Alternatively, pyroelectric energy converters offer a novel, direct energy-conversion technology by transforming time-dependent temperatures directly into electricity [2–9]. It makes use of the pyroelectric effect to create a flow of charge to or from the surface of a material as a result of heating or cooling [10]. Indeed, in response to temporal changes in temperature, positive and negative charges move to opposite ends, establishing an electrical potential across the materials. The fact that very small changes in temperature (~m K) can produce a pyroelectric current in the order of nA or pA [10] has been used extensively in infrared detectors for imaging and motion sensors as well as thermometers [11]. However, little effort has been made to use them for direct energy conversion.

Prototypical pyroelectric converters have been assembled and operated in the past [2–9]. However, to the best of our knowledge, only a simplified numerical analysis has been performed to optimize the thermodynamic energy efficiency of the system [12]. Many assumptions and simplifications were made presumably due to limited computer resources and resulted in poor agreement with experimental data for certain operating conditions [12]. This paper reports, for the first time, complete numerical simulations of a prototypical pyroelectric converter experimentally assembled by Olsen et al. [2] in order to identify key design and operating parameters to increase the power output and the thermodynamic efficiency of the device.

2. Current state of knowledge

2.1. Pyroelectric materials

Pyroelectric materials are materials whose spontaneous polarization presents strong temperature dependence due to their crystallographic structure [10]. The displacement of the atoms from their equilibrium positions upon heating and cooling gives rise to spontaneous polarization resulting in the pyroelectric effect. At steady-state ($dT/dt = 0$), the spontaneous polarization is constant and no current is flowing. However, a rise in temperature ($dT/dt > 0$) reduces the spontaneous polarization through reduction in the dipole moment. The number of bound charges decreases and the subsequent redistribution of charges results in current flowing

* Corresponding author. Tel.: +1 310 206 5598.
E-mail address: pilon@seas.ucla.edu (L. Pilon).

0017-9310/$ - see front matter © 2008 Elsevier Ltd. All rights reserved.
doi:10.1016/j.ijheatmasstransfer.2008.04.008

Nomenclature

A	surface area of pyroelectric element, m^2
A_C	cross-sectional area of fluid flow for one channel, m^2
A_{hb}	area of heating band ($d \times L_H$), m^2
A_p	cross-sectional area of piston, m^2
Bi	Biot number
C	capacitor, F
c_p	Specific heat at constant pressure, J/kg K
d	channel depth, m
D_h	hydraulic diameter (=$4w_f$), m
f	frequency, 1/s
g	gravity, m/s^2
h_ω	heat transfer coefficient in oscillating flow, W/m^2 K
k	thermal conductivity, W/m K
L	total length of wall, m
L_C	length of heat exchanger, m
L_H	length of heating band, m
L_{cr}	length of aluminum oxide plate, m
N	number of walls with pyroelectric elements
p	pressure, Pa
p_0	atmospheric pressure at free surface, Pa
P_D	power density, W/L
PE	pyroelectric element
q''_{in}	heat flux at heating band, W/m^2
q	charge, C/m^2
$\dot{Q}_{in}$	heat transfer rate into the pyroelectric converter, W
R_2	input current resistance, Ω
R_D	voltage divider resistance, Ω
Re	Reynolds number for oscillating flow ($= 2\pi f D_h^2/4\nu_f$)
S	amplitude of piston oscillation, m
S'	amplitude of working fluid in channel, m
t	time, s
T	temperature, °C or K
T_{Curie}	Curie temperature, °C
T_C	temperature of cold source, °C
T_{cool}	cold temperature of the pyroelectric element, °C
T_H	temperature of hot source, °C
T_{hot}	hot temperature of the pyroelectric element, °C
ΔT	temperature swing, °C
u	velocity in the x-direction, m/s
v	velocity in the z-direction, m/s
V	voltage, V
V_L	low applied voltage, V
V_H	high applied voltage, V
$\mathbf{V}$	volume, m^3
w	half-width, m
$\dot{W}_E$	generated electrical power, W
$\dot{W}_p$	pumping power, W
x	transverse coordinate in (x,z) coordinate system
z	vertical coordinate in (x,z) coordinate system
z_h	distance from transverse axis to heating band, m

Greek symbols

η	thermodynamic efficiency, %
η_{Carnot}	Carnot efficiency, %
ν	kinematic viscosity, m^2/s
ρ	density, kg/m^3
τ	period of oscillation, (=$1/f$), s
τ_t	thermal time constant, s

Subscripts

A	refers to point A
B	refers to point B
cr	refers to aluminum oxide plate
f	refers to working fluid
p	refers to piston
PE	refers to pyroelectric element
w	refers to wall

through the external circuit. If the sample is cooled, the current sign is reversed.

In addition, the relationship between the charge q and the open-circuit voltage V at constant temperature features a hysteresis loop as illustrated in Fig. 1 for lead zirconate stannate titanate, $Pb_{0.99}Nb_{0.02}(Zr_{0.68}, Sn_{0.25}, Ti_{0.07})_{0.98}O_3$ (PZST), between 152 °C and 194 °C. The surface area of the loop represents the electric losses if it is cycled counter-clockwise. Note that the spontaneous polarization vanishes beyond the Curie temperature denoted by T_{Curie}.

2.2. Pyroelectric energy conversion

A quasi-isothermal cycle ($\Delta T \sim$ m K) of the voltage produces very low power and features very low efficiencies [13]. However, by removing the quasi-isothermal constraints, pyroelectric energy conversion is possible by alternatively placing the pyroelectric material sandwiched between two electrodes in contact with a hot and a cold thermal reservoir and imposing the proper voltage as illustrated in Fig. 1 with the Olsen cycle represented by the cycle 1–2–3–4. Unfortunately, this process is highly irreversible and theoretical analysis predicts low efficiency and small output power [13,14]. However, this low efficiency can be significantly improved by using (1) multistaging and (2) heat regeneration during the cycle [2,3]. Multistaging consists of placing different pyroelectric materials in series with increasing Curie temperatures from the cold to the hot sources along the oscillating flow. In addition, the

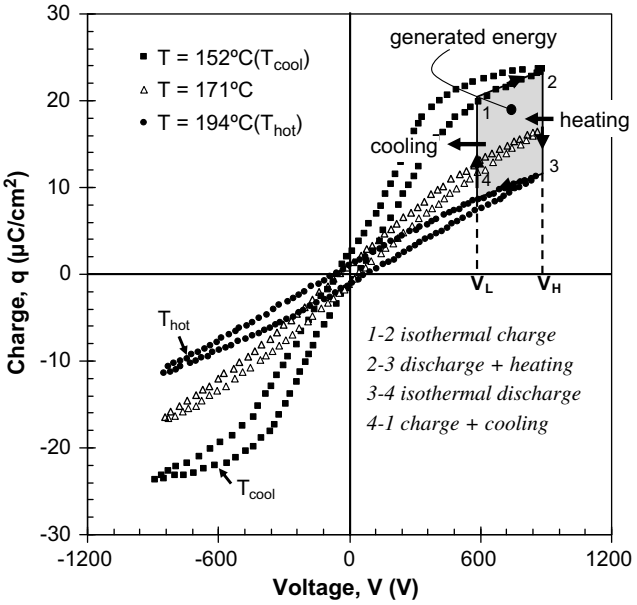

Fig. 1. Polarization vs. applied voltage curves for PZST at different temperatures below $T_{Curie} = 240$ °C. The Olsen power cycle is represented by the area between 1–2 and 3–4.

heat required to increase the temperature of the lattice is regenerated back and forth between the working fluid and the pyroelectric elements (PEs), like in a Stirling engine, instead of being lost to the heat sink.

Finally, it has been established theoretically that pyroelectric conversion based on heat regeneration using an oscillating working fluid and the Olsen cycle can reach the Carnot efficiency between a hot and a cold thermal reservoir [7]. Limitations in reaching the Carnot efficiency include (i) leakage current, (ii) heat losses to the surrounding, and (iii) sensible (thermal) energy required to heat the pyroelectric material. Olsen et al. [15] predicted that "the limit of conversion efficiency due to the ferroelectric material (for an ideal engine) is 84–92% of the Carnot".

To the best of our knowledge, only seven prototypical pyroelectric converters have been built to date. First, Olsen et al. [4–6] experimentally demonstrated 1 mW and 40 mW devices with efficiency around 0.4% but 16 times greater than the maximum efficiency predicted by van der Ziel [14]. They used PZST as the pyroelectric materials and silicone oil as the working fluid while they operated between cold and hot sources at temperatures $T_C = 145$ °C and $T_H = 178$ °C, respectively [4]. Ceramic stacks [2–6] and spacers [7] were used to form microchannels which ensure periodically oscillating laminar flow of the working fluid over the ceramic and pyroelectric elements. Indeed, turbulence would result in mixing of the cold and hot fluid and disrupt the temperature gradient oscillating in the column. Later, Olsen et al. [2] assembled the only multistage device built to date, using PZST doped with Ti^{4+} and Sn^{4+} resulting in different T_{Curie} for a maximum power output of 33 W per liter of pyroelectric materials at 0.26 Hz and featuring a maximum thermodynamic efficiency of 1.05% at 0.14 Hz. The system was operated between 145 °C and 185 °C. However, due to the cost of PZST (~$10,000/W), Olsen et al. [7] proposed to use inexpensive single stage 30–70 μm thick PVDF films sandwiched between electrodes and rolled in a spiral stack placed into a cylindrical chamber containing silicone oil. The electrical output between $T_C = 20$ °C and $T_H = 90$ °C achieved was 30 J/L of PVDF per cycle, or period of oscillation of the working fluid. In all the prototypes [2–7], the pumping was performed by a step motor with a piston peak-to-peak stroke length varying from 7.8 to 10 cm.

More recently, Ikura [8] built a pyroelectric converter using a single 60–40% P(VF_2–TrFE) film where hot and cold water is alternatively flowed over the film assembly. The water temperature ranged from 58 °C to 77 °C at a period of oscillation of 3.9 s resulting in an energy density between 15 and 52 J/L of copolymer per cycle. Later, using the same set up, Kouchachvili and Ikura [9] achieved an energy density of 279 J/L per cycle using a purified 60–40% P(VDF–TrFE) film. Kouchachvili and Ikura [8,9] focused on reducing the leakage current of the pyroelectric material. Note that the frequency, temperature range, electrode material, and working fluid were not disclosed.

Numerical simulations of a pyroelectric converter were also performed by Olsen et al. [12]. The heat transfer rate and temperature variations of the PZST pyroelectric material within the converter were determined for peak-to-peak stroke lengths of 2.8, 5.1, and 8.5 cm and frequencies ranging from 0 to 0.6 Hz. The authors solved only the energy equation assuming that (1) all of the channel walls were made of aluminum oxide only, (2) the flow was one-dimensional, laminar, fully developed oscillating flow with a parabolic velocity profile across the converter's channel, (3) axial heat conduction along the converter's walls was negligible, and (4) the heating and cooling heat exchangers were at constant temperatures and placed directly above and below the pyroelectric material. Olsen et al. [12] found that the numerical predictions of the heat transfer rate agree well with the experimental results at all frequencies for stroke lengths smaller than 2.24 cm but became increasingly inaccurate (by up to 50%) for larger stroke lengths. This can be attributed to the simplifying assumptions previously listed. Indeed, the velocity profile of the working fluid is not fully developed along the microchannels but instead is constant across the channel width at the entrance. In addition, axial heat conduction takes place along the composite wall between the hot and cold sources, and the hot source operated at constant heat flux and not at constant temperature as simulated numerically in Ref. [12]. Finally, the heating and cooling heat exchangers are not directly above and below the pyroelectric plates as assumed in Ref. [12]. Instead, in the actual prototype [2], they are separated by 1.905 and 5.08 cm of aluminum oxide, respectively.

The aim of this paper is (1) to assess the numerical approach taken by Olsen et al. [12] against a more complete formulation made possible by the development of advanced numerical methods and greater computational resources, and (2) to identify the operating frequency, working fluid, and pyroelectric material that would enable larger energy efficiency and/or power output.

3. Analysis

3.1. Direct pyroelectric conversion system

3.1.1. Thermal sub-system

Fig. 2 shows a cross-section of the simulated prototypical two-stage pyroelectric converter [2] along with the dimensions and the associated coordinate system. The working fluid oscillates vertically between N stationary equidistant walls forming $(N + 1)$ channels. All walls are identical and comprised of four plates placed vertically along the direction of the fluid flow. The top and bottom plates are made of aluminum oxide, while the center two plates are made of PZST and are forming the active region of the device. A heat exchanger located at the bottom of the test section cools the working fluid at constant temperature T_C. In addition, a thin heating band is located in the middle of the channel at the top of the test section. It heats the working fluid and operates at constant heat flux $q''_{in} = 664\ q''_{in}$. The half-widths of the flow channel and of the wall are denoted by w_f and w_w, respectively. The total length of the channel is denoted by L while L_{cr} is the length of each of the lower and upper aluminum oxide plates. The bottom of the heating band is located at height z_h, and the length of the heat exchanger and heating band are denoted by L_C and L_H, respectively (see Fig. 2). The heating band is simulated as a line source located in the middle of the channel. In addition, points A and B are located at the center of the pyroelectric elements PE_1 and PE_2 and height z_A and z_B, respectively. Moreover, the height from the bottom of the test section to the top of PE_1 and bottom of PE_2 is $z_1 = (L - L_{cr})$ and $z_2 = (L_C + L_{cr})$, respectively. Finally, the entire pyroelectric converter has a depth $d = 3.8$ cm [2]. The oscillation of the fluid flow through the minichannel is achieved via a piston-in-a-cylinder pump with adjustable piston amplitude S and frequency f. At time t, the piston top surface is located at $z_p = -S[1 + \cos(2\pi ft)]$, where, initially $(t = 0)$, the piston is at its lowest position at $z_p(0) = -2S$ and the liquid free surface is located at $z = L$.

3.1.2. Electrical sub-system

The electric sub-system used for a single pyroelectric element was obtained from Olsen et al. [3] and is shown in Fig. 3. It is relatively simple but essential for achieving the desired thermodynamic cycle shown in Fig. 1. To do so, both faces of each pyroelectric thin-film are plated with electrodes and connected to the electrical sub-system. The charge from the pyroelectric elements and the applied voltage are measured from the voltage drop across capacitor C and resistor R_2, respectively. Resistor R_D serves as a voltage divider to scale down current signals to match the

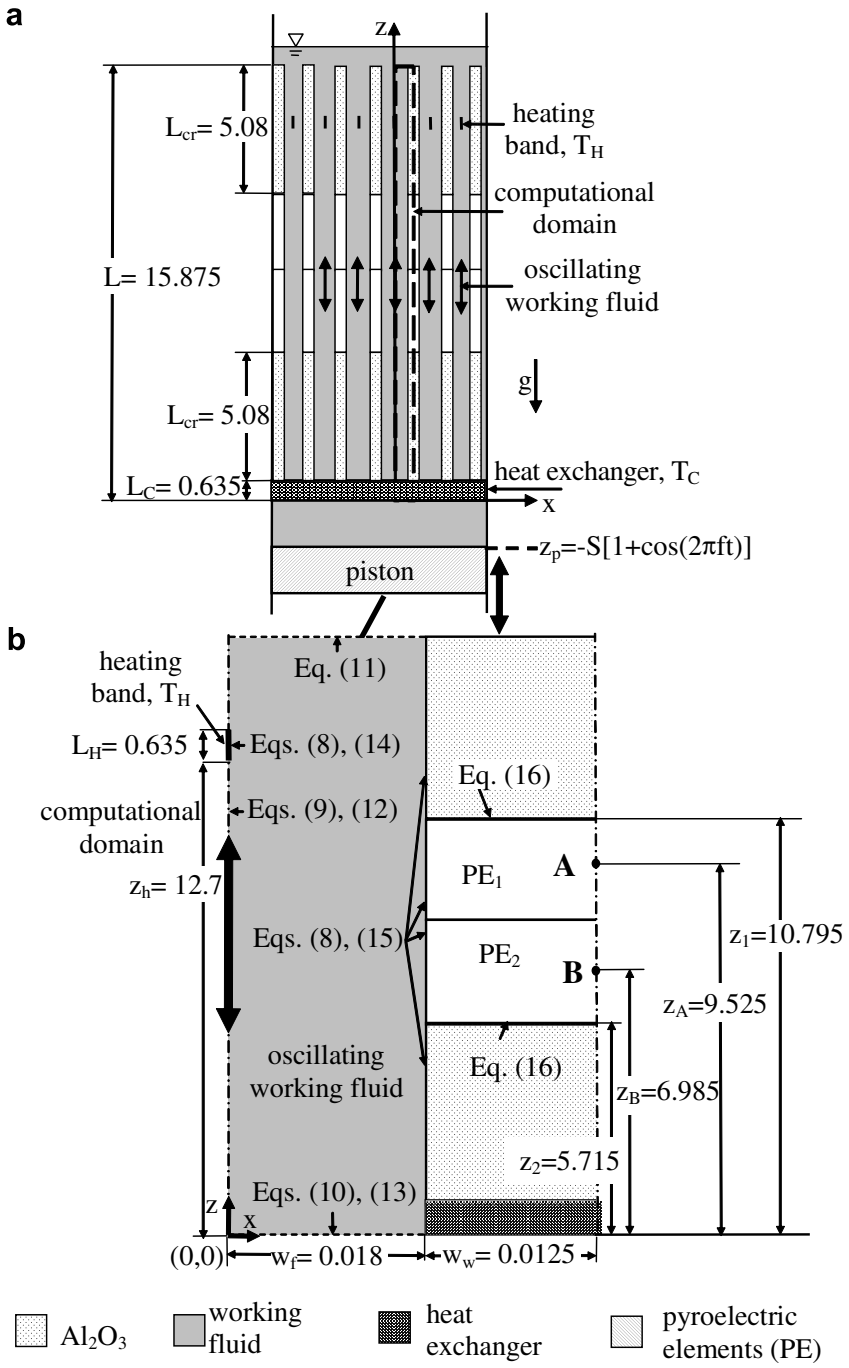

Fig. 2. (a) Schematic of the overall pyroelectric converter, (b) schematic of the computational domain along with the coordinate axis and the boundary conditions (all dimensions in cm).

input limits of the instruments. Voltages V_L and V_H are supplied in order to maintain the desired low or high voltages required for the Olsen cycle represented in Fig. 1. The temperature and voltage of each pyroelectric element are synchronized using a switch to produce the cycle. Each switch is actuated whenever the temperature of the pyroelectric element reaches a maximum or a minimum thanks to a control system. Referring to Fig. 1, the isothermal charge 1–2 of the pyroelectric element at constant temperature T_{cool} is provided by the power supply switching from V_L to V_H. The pyroelectric element is then heated (2–3) at constant voltage V_H up to temperature constant T_{hot}. It is then isothermally discharged in the load (3–4) by switching the voltage from V_H to V_L. Finally, the cycle is closed by cooling the pyroelectric element at constant voltage V_L.

3.2. Assumptions

To make the problem mathematically trackable the following assumptions are made:

1. The entire pyroelectric converter is well insulated so heat losses to the surrounding and between channels are negligible.
2. All material properties for the wall and the working fluid are assumed to be constant and isotropic.

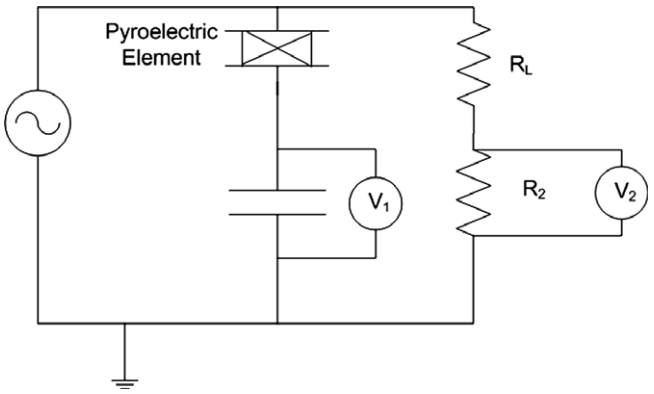

Fig. 3. Electrical sub-system for each pyroelectric element [8].

3. The working fluid is silicone oil Dow Corning 50 cst which is treated as a Newtonian and incompressible fluid.
4. The spacing between the walls is much smaller than the depth of the plate so that two-dimensional flow prevails.
5. The Reynolds number of the periodically oscillating fluid flow, defined as $Re(f) = 2\pi f D_h^2/4\nu_f$, is less than 0.02 for all simulations so that fluid flow is laminar [16].
6. The relationship between the charge q and the open-circuit voltage V at constant temperature features a hysteresis curve as shown in Fig. 1.
7. Edge effects are neglected. In other words, all channels are equivalent and only one is considered.
8. As a first order approximation, the electrodes deposited on the PE plates to collect the generated current are assumed to have no effect on the heat transfer and fluid flow.
9. Due to the lack of thermophysical properties for various doping levels of PZST, the PEs at the two stages of the converter are assumed to be identical.

3.3. Governing equations

The components of the velocity vector and the pressure field of the working fluid are calculated by solving the two-dimensional mass and momentum conservation equations expressed for an incompressible and Newtonian fluid with constant properties in Cartesian coordinates as [17],

$$\frac{\partial u_f}{\partial x} + \frac{\partial v_f}{\partial z} = 0 \tag{1}$$

$$\frac{\partial u_f}{\partial t} + u_f\frac{\partial u_f}{\partial x} + v_f\frac{\partial u_f}{\partial z} = -\frac{1}{\rho_f}\frac{\partial p_f}{\partial x} + \nu_f\left(\frac{\partial^2 u_f}{\partial x^2} + \frac{\partial^2 u_f}{\partial z^2}\right) \tag{2}$$

$$\frac{\partial v_f}{\partial t} + u_f\frac{\partial v_f}{\partial x} + v_f\frac{\partial v_f}{\partial z} = -\frac{1}{\rho_f}\frac{\partial p_f}{\partial z} + \nu_f\left(\frac{\partial^2 v_f}{\partial x^2} + \frac{\partial^2 v_f}{\partial z^2}\right) - g \tag{3}$$

where ρ_f and ν_f are the density and kinematic viscosity of the working fluid, while u_f and v_f are the components of the fluid velocity vector in the x- and z-directions, respectively. The pressure of the working fluid is denoted by p_f and g is the gravitational acceleration equal to 9.81 m/s^2 acting along the z-axis oriented upward.

The two-dimensional energy equation solved to determine the temperature distribution within the working fluid is written as [17],

$$\rho_f c_{p,f}\left(\frac{\partial T_f}{\partial t} + u_f\frac{\partial T_f}{\partial x} + v_f\frac{\partial T_f}{\partial z}\right) = k_f\left(\frac{\partial^2 T_f}{\partial x^2} + \frac{\partial^2 T_f}{\partial z^2}\right) \tag{4}$$

where $c_{p,f}$ is the heat capacity of the fluid, T_f is the local fluid temperature, and k_f is the fluid thermal conductivity, assumed to be constant.

Similarly, the two-dimensional heat diffusion equation for the aluminum oxide and PZST plates constituting the channel walls is expressed as,

$$\rho_w c_{p,w}\frac{\partial T_w}{\partial t} = k_w\left(\frac{\partial^2 T_w}{\partial x^2} + \frac{\partial^2 T_w}{\partial z^2}\right) \tag{5}$$

where the subscript w refers to either the aluminum plates or to the pyroelectric elements.

3.4. Initial and boundary conditions

At time $t = 0$, the working fluid is assumed to be at rest, i.e., for $0 < x < w_f$ and $0 < z < L$,

$$u_f(x,z,0) = v_f(x,z,0) = 0 \tag{6}$$

Initially, the temperature throughout both the walls and the working fluid does not vary in the x-direction (i.e., for $0 < x < w_f + w_w$) and is linear between the heating band at location $z = z_h$ and temperature T_H and the heat exchanger at location $z = L_C$ and temperature T_C. In addition, the temperature profile of the working fluid remains constant along and above the heat exchanger and along the heating band, so that for $0 < x < w_f + w_w$,

$$T_f(x,z,0) = T_w = \begin{cases} T_C & \text{for } 0 \leqslant z \leqslant L_C \\ T_C + \frac{(T_H - T_C)(z - L_C)}{z_h - L_C} & \text{for } L_C \leqslant z \leqslant z_h \\ T_H & \text{for } z_h \leqslant z \leqslant L \end{cases} \tag{7}$$

For later times t, the no-slip condition prevails at the wall ($x = w_f$) and heating band ($x = 0$). Thus, the velocity components $u_f(x,z,t)$ and $v_f(x,z,t)$ are such that,

$$\begin{aligned} &u_f(w_f,z,t) = v_f(w_f,z,t) = 0 \quad \text{for } 0 \leqslant z \leqslant L \\ &u_f(0,z,t) = v_f(0,z,t) = 0 \quad \text{for } z_h \leqslant z \leqslant (z_h + L_H) \end{aligned} \tag{8}$$

On the other hand, the symmetry boundary condition is imposed at the channel centerline ($x = 0$), i.e.,

$$u_f(0,z,t) = \frac{\partial v_f}{\partial x}(0,z,t) = 0 \quad \text{for } 0 \leqslant z \leqslant z_h, (z_h + L_H) \leqslant z \leqslant L \tag{9}$$

In addition, the velocity of the working fluid at the piston is equal to the velocity of the piston, given by $v_p = 2\pi f S\sin(2\pi f t)$. From mass conservation considerations and assuming that the fluid is incompressible, the velocity at the bottom of the microchannels is uniform and a sinusoidal function of time with amplitude $S' = SA_P/[(N+1)A_c]$, i.e.,

$$u_f(x,0,t) = 0, v_f(x,0,t) = 2\pi f S'\sin(2\pi f t) \quad \text{for } 0 \leqslant x \leqslant w_f \tag{10}$$

where A_p and A_C are the cross-sectional area of the piston and of a single channel, respectively.

The incompressible working fluid above the channel oscillates with the same amplitude and frequency as the piston such that the free surface oscillates between $z = L$ and $z = L + 2S$ as the piston moves from $z_p = -2S$ to $z_p = 0$, respectively. In addition, since the cross-sectional area of the working fluid at the top of the reservoir above $z = L$ is large and equal to that of the piston A_p, the pressure at $z = L$ can be assumed to be dominated by hydrostatic pressure and given by,

$$p_f(x,L,t) - p_0 = \rho_f g S[1 - \cos(2\pi f t)] \quad \text{for } 0 \leqslant x \leqslant w_f \tag{11}$$

where p_0 is the atmospheric pressure at the free surface.

The symmetry boundary condition is used for the temperature at the centerline of the wall and of the flow channel resulting in,

$$\frac{\partial T_f}{\partial x}(0,z,t) = \frac{\partial T_f}{\partial x}(w_f + w_w, z, t) = 0 \quad \text{for } 0 \leqslant z \leqslant L \tag{12}$$

In addition, the temperature of the working fluid at $z = 0$ is constant and equal to the temperature of the heat exchanger T_C across the channel so that

$$T_C = T_f(x, 0, t) \quad \text{for } 0 \leqslant x \leqslant w_f \tag{13}$$

Likewise, the heat flux along the heating band surface is constant and equal to q''_{in}, i.e.,

$$q''(0, z, t) = q''_{in} \quad \text{for } z_h \leqslant z \leqslant (z_h + L_H) \tag{14}$$

where q''_{in} is adjusted to achieve the desired temperature T_H at the heating band. Moreover, the heat fluxes normal to the flow direction at the interfaces between the working fluid and either the PE or the aluminum oxide plates are expressed as,

$$-k_f \frac{\partial T_f}{\partial x}(w_f, z, t) = -k_w \frac{\partial T_w}{\partial x}(w_f, z, t) \quad \text{for } 0 \leqslant z \leqslant L \tag{15}$$

Finally, the axial heat transferred by conduction between the PEs and the aluminum oxide plates is accounted for by equating the axial heat fluxes on both sides of the interfaces located at z_1 and z_2,

$$-k_{cr} \frac{\partial T_{cr}}{\partial x}(x, z_1 \text{ or } z_2, t) = -k_{PE} \frac{\partial T_{PE}}{\partial x}(x, z_1 \text{ or } z_2, t) \quad \text{for } w_f \leqslant x \leqslant w_f + w_w \tag{16}$$

3.5. Properties

The thermophysical properties of aluminum oxide, PZST, and of the working fluid are assumed to be constant over the temperature range simulated. This assumption is justified by the fact that the relative differences in the materials properties are less than 10% between $T_C = 145$ °C and $T_H = 185$ °C except for the kinematic viscosity of the working fluid v_f which varies by up to 37%. As a first order approximation, v_f is assumed to be constant and equal to 8.29 mm^2/s [18] taken at the arithmetic mean temperature of 165 °C. The density, specific heat, and thermal conductivity of Al_2O_3 and silicone oil are also estimated at the arithmetic mean temperature of 165 °C and obtained from Ref. [19] and Refs. [18,20], respectively. Unfortunately, the density, specific heat, and thermal conductivity of PZST could only be obtained from the literature at room temperature [21]. However, its charge–voltage curve was estimated at the temperature computed in the pyroelectric elements PE_1 and PE_2. Table 1 summarizes the values of the material properties of aluminum oxide, PZST, and the working fluid used to solve the above governing equations.

3.6. Method of solution

The local velocity, pressure, and temperature throughout the computational domain are determined by solving the mass, momentum, and energy equations (Eqs. (1)–(5)) along with their associated initial boundary conditions (Eqs. (6)–(16)). At every time step, the mass and momentum conservation equations are solved simultaneously using the finite element solver FEMLAB 3.0 applying the Galerkin finite element method on unstructured meshes. Then, the energy equation is solved for the fluid as well as for the aluminum oxide and pyroelectric elements. A Dell Precision 690 with eight 2.66 GHz processors, and 8 GB of RAM is used to run the simulations. Note that the choice of the equation solver is arbitrary.

Table 1
List of fluid and material properties used in numerical simulation (Case 1) [18–21]

Properties	Silicone oil (50 cst) at 165 °C	PZST [21] at 25 °C	Al_2O_3 [19] at 165 °C
ρ (kg/m^3)	761.6 [18]	7750	3970
c_p (J/kg K)	1913.3 [18]	350	972.4
k (W/m K)	0.157 [20]	1.1	24.4
v_f (mm^2/s)	8.29 [18]	–	–

The internal time step is chosen arbitrarily to ensure numerical stability in solving the mass, momentum, and energy equations. On the other hand, the result is recorded at time intervals Δt such that $2\pi f \Delta t = \pi/2$ for all frequencies unless otherwise mentioned. Numerical convergence is established by solving the governing equations with a coarse grid and a grid size 1.3 times smaller. The results are assumed to be numerically converged when the maximum relative difference in the local velocity, pressure, and temperature throughout the computational domain is less than 0.5%, 0.1%, and 1.8%, respectively, between two consecutive grid refinements for all frequencies.

For validation purposes, the numerical results for velocity and pressure for vertically oscillating adiabatic flow were compared with the analytical solution for fully developed laminar flow expressed as [22],

$$u_f(x, z, t) = 0, v_f(x, z, t) = 3\pi f S' \left[1 - \left(\frac{x}{w_f}\right)^2\right] \sin(2\pi f t) \tag{17}$$

The numerical results fall within 1.05% of the above analytical solution at all points for $0 \leqslant x \leqslant w_f$ and for $0 \leqslant z \leqslant L$. Moreover, the numerical results for pressure and temperature in unidirectional, fully developed laminar flow with a well-known parabolic velocity profile and constant wall heat flux were compared with the analytical solution [19]. The maximum relative difference for pressure and temperature was found to be 0.007% and 0.43%, respectively. This validates the numerical simulation tool and proper implementation of the governing equations and boundary conditions.

4. Results and discussion

4.1. Comparisons of approach

Let us consider a pyroelectric converter with the geometry and dimensions shown in Fig. 2. The cold heat exchanger is at constant temperature $T_C = 145$ °C. The heating band operates at constant heat flux $q''_{in} = 664$ W/m^2 in order to achieve $T_H = 185$ °C. The cross-sectional area of the fluid flow through one minichannel is $A_C = 0.137$ cm^2 while that of the piston is $A_p = 23.317$ cm^2. The piston driving the fluid oscillates with a frequency $f = 0.081$ Hz and amplitude $S = 3.9$ cm. The optimum piston amplitude is such that a fluid particle located in front of the heating band at $z = (z_h + L_H)$ when the piston is at its maximum height $z_p = 0$ carries its thermal energy down to location $z = z_2$ when the piston is at its lowest point $z_p = -2S$. Larger piston amplitudes would result in heat losses as opposed to heat regeneration by the active region. Smaller amplitudes would lead to lower temperature swings in the PEs. In both cases, the power generated would not be at a maximum. Thus, the optimum stroke length is expressed as cm. Therefore, the stroke length of $S = 3.9$ cm chosen experimentally by Olsen et al. [2] is close to optimum and used in our simulation.

For the sake of simplicity, Olsen et al. [12] numerically computed the temperature profiles of a pyroelectric converter by solving the energy equation and assuming a fully developed laminar flow velocity profile given by Eq. (17) along the minichannels. Their approach is referred to as Approach 1. However, at the bottom of the ceramic stack located at $z = 0$ (see Fig. 2), the velocity profile is not fully developed but uniform and oscillating across the channel width (Eq. (10)). Approach 2 consists of solving the mass, momentum, and energy conservation equations with the associated boundary conditions. The predictions obtained between these two different approaches are compared to assess the validity of Olsen et al.'s assumptions [12]. This would enable system

optimization through accurate and efficient numerical simulation of actual pyroelectric converters.

4.1.1. Velocity profile

Fig. 4a and b show the fluid velocity component v_f across the channel as predicted by Approaches 1 and 2 for frequency $f = 0.081$ Hz (a) at $z = 0$ m and (b) at $z = z_B$, respectively. Different times are considered namely (i) $2\pi ft = \pi/2 + n\pi$ when the piston is at $z_p = -S$, (ii) $2\pi ft = n\pi$ when the piston is at the middle point $z_p = 0$ or $-2S$, and (iii) $2\pi ft = \pi/4 + n\pi/2$ when the piston is at $z_p = -(1 \pm \sqrt{2}/2)S$, where n is an integer. Note that the velocity profile at $z = z_A$ is identical to that at $z = z_B$ and need not be shown. Fig. 4 indicates that the velocity profile across the channel varies significantly from the bottom of the channel ($z = 0$) to the pyroelectric elements ($z = z_B$). At $z = z_B$ the results for Approaches 1 and 2 are superimposed. However, the flow is fully developed at all times when it reaches either stage of pyroelectric elements. The relative difference in the local velocity component v_f between Approaches 1 and 2 is within 1.05% at $z = z_B$ but reaches up to 72% at $z = 0$ m. The difference observed at the level of the pyroelectric materials might appear acceptable. However, it results in large differences in temperature oscillations of the pyroelectric elements as discussed later. Note that the fluid velocity profile of Approach 2 appears to be non-zero along the channel wall ($x = w_f$) in Fig. 4a. In fact, $v_f(w_f,0)$=0, but the velocity gradient is large.

4.1.2. Pressure distribution

Numerical results indicate that the pressure is nearly uniform across the channel width and reaches periodic steady-state very quickly. Fig. 5 shows the temporal evolution of the gauge pressure across the channel at the bottom of the microchannel ($z = 0$) predicted by Approach 2 only. Indeed, Approach 1 solves only for the energy equation and does not predict the fluid pressure. Fig. 5 establishes that the average pressure at $z = 0$ is a sinusoidal function of time at the imposed piston frequency of 0.081 Hz with amplitude 3482.3 Pa around a mean value of 1477.4 Pa. The mean value falls within 0.01% of the time-averaged hydrostatic pressure given by Eq. (11) and expressed as,

$$\bar{p}_f(x,0,t) - p_0 = \rho_f g(L+S) \tag{18}$$

4.1.3. Temperature distribution

Fig. 6 compares the temperature in the pyroelectric elements PE_1 and PE_2 at points A and B, respectively, predicted by both approaches as a function of time for frequency $f = 0.081$ Hz. The predicted temperature is a sinusoidal function of time oscillating between T_{hot} and T_{cool} at a frequency identical to that of the piston. After approximately $t = 1100$ s, the temperature predicted by Approaches 1 and 2 reaches periodic steady-state. Note that Approach 2 predicts a much more regular periodic oscillation compared with Approach 1. Approach 2 predicts that the temperature oscillates approximately between 166.1 °C and 183.5 °C at point A [$\Delta T_A = T_{hot,A} - T_{cool,A} = 17.4$ °C] and between 156.0 °C and 178.4 °C at point B [$\Delta T_B = T_{hot,B} - T_{cool,B} = 12.4$ °C]. The largest relative difference in the temperature predicted by Approaches 1 and 2 is 12.2% and 11.8% for points A and B, respectively. However, this corresponds to an absolute error in temperature of 22.1 °C and 21.0 °C at points A and B, respectively. Such a large absolute difference can result in large differences in the predicted electrical power generated and in the efficiency. Thus, the mass, momentum, and energy

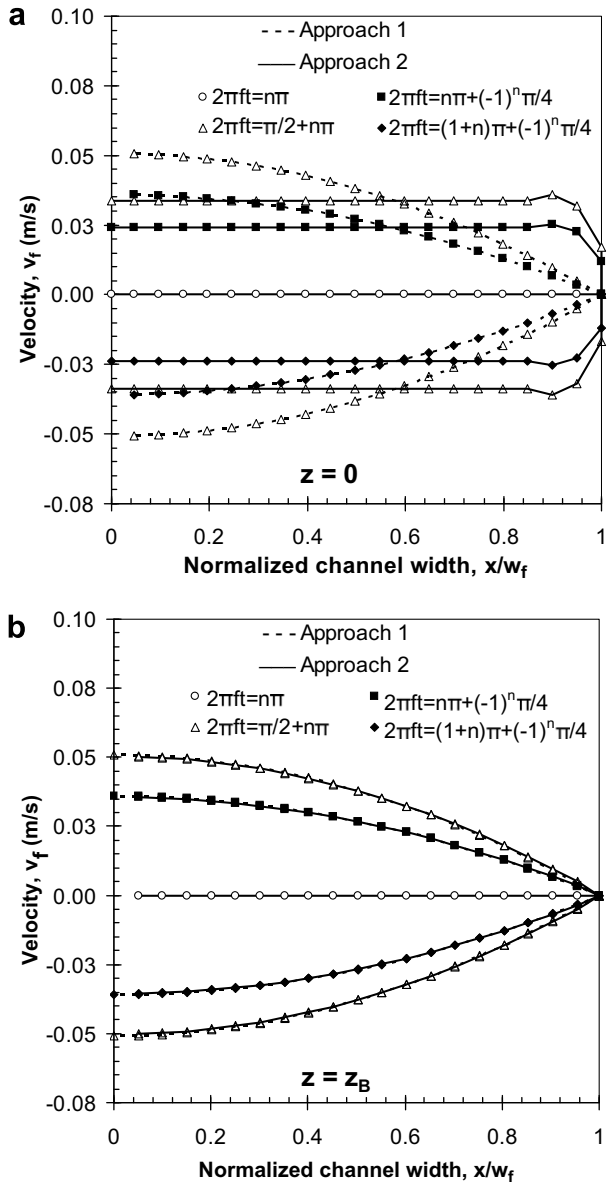

Fig. 4. Fluid velocity distribution across the channel at various times for Approaches 1 and 2 (a) at $z = 0$ and (b) at $z = z_B$ (n is an integer).

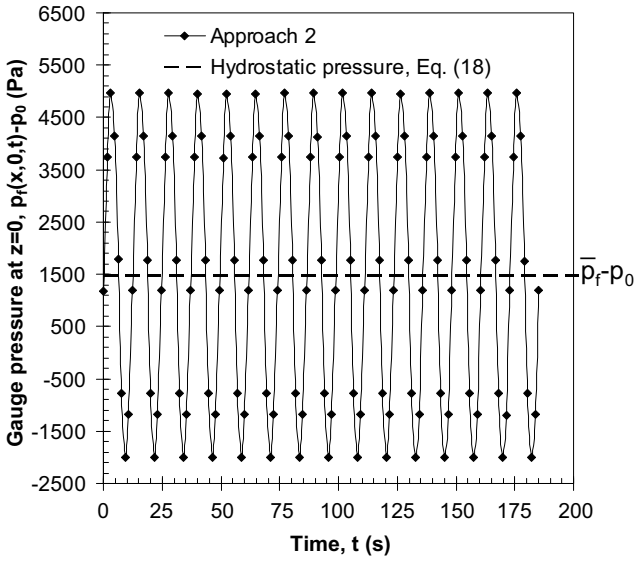

Fig. 5. Sinusoidal evolution of the fluid pressure as a function of time at location $z = 0$ predicted by Approach 2.

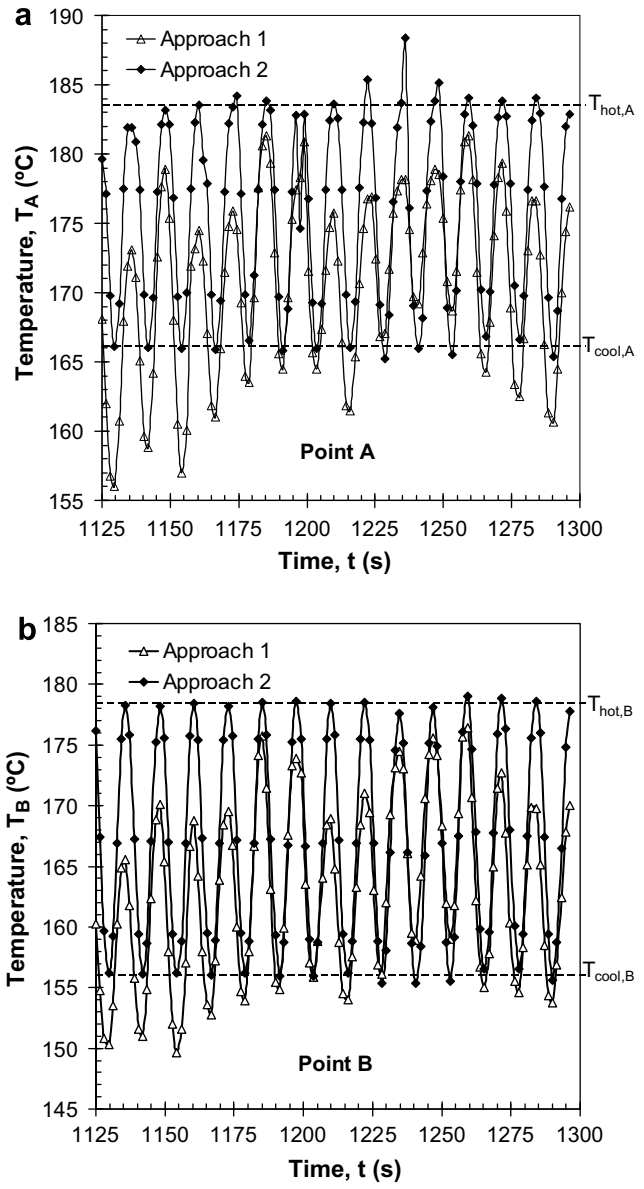

Fig. 6. Temperature obtained from Approaches 1 and 2 as a function of time at (a) point A and (b) point B.

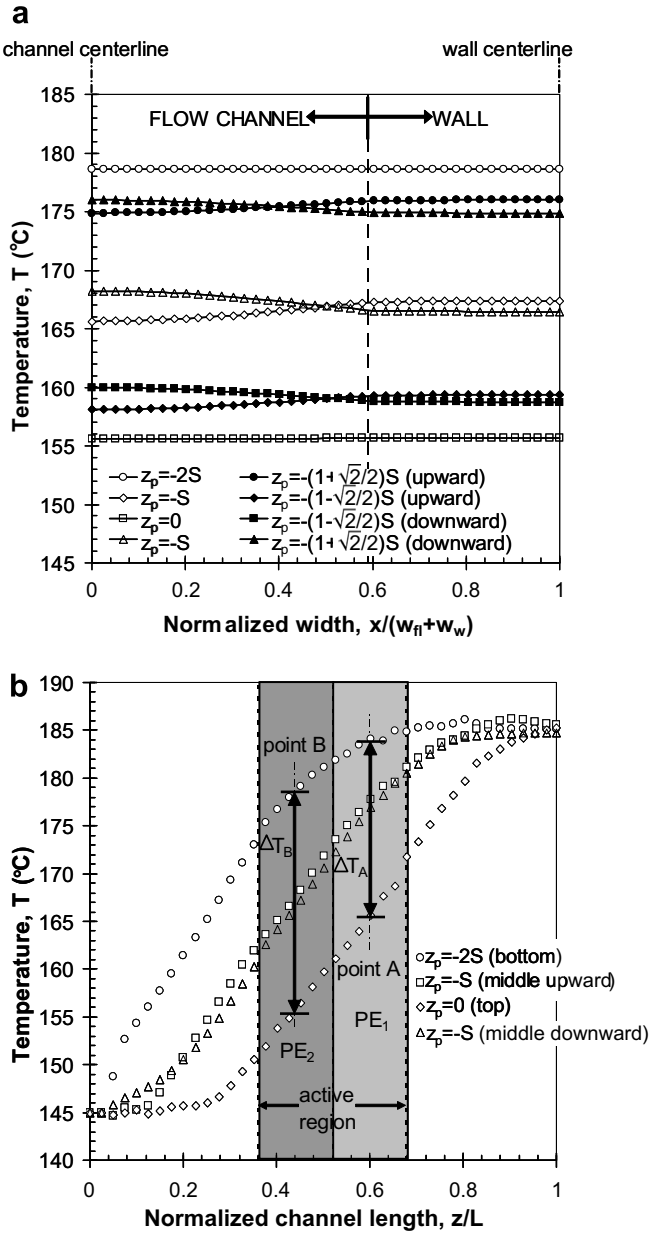

Fig. 7. (a) Temperature at height $z = z_B$ across the flow channel and the wall for f = 0.081 Hz and multiple piston positions and (b) temperature at $x = (w_f + w_w)$ along the wall centerline for f = 0.081 Hz and multiple piston positions.

equations must be solved at all times, and Approach 2 is used in the remainder of the study. Fig. 6 also establishes that the converter will operate most efficiently if the pyroelectric materials chosen for the lower (PE_2) and upper (PE_1) pyroelectric elements have Curie temperatures equal to $T_{cool,A} = 166.1\,^{\circ}C$ and $T_{cool,B} = 156.0\,^{\circ}C$, respectively.

Fig. 7a shows the temperature distribution at height $z = z_B$ across the fluid channel and the wall for f = 0.081 Hz and multiple piston positions. It indicates that the temperature of the wall is uniform across its half-width for every time step. Indeed, the Biot number for PE_1 and PE_2, defined as $Bi = h_\omega w_w / k_{PE}$ where h_ω is the time-dependent heat transfer coefficient between the fluid and the PEs, is much smaller than unity. In addition, the amplitudes of the temperature oscillations in the fluid and in the wall are nearly identical.

Similarly, Fig. 7b shows the wall temperature distribution at the wall centerline (at $x = w_f + w_w$) at frequency f = 0.081 Hz for multiple piston positions. It establishes that the temperature swing at point A is smaller than that at point B. In addition, Fig. 7b enables the designer to properly place the multistage pyroelectric elements with different Curie temperatures and to predict their minimum and maximum operating temperatures.

4.2. Effect of frequency on temperature oscillations

Numerical simulations similar to those performed previously are done using Approach 2 for frequency f equal to 0.01, 0.031, 0.062, 0.112, 0.137, and 0.2 Hz for a piston amplitude of S = 3.9 cm. In all cases, the heat flux q''_{in} was adjusted by trial and error in order to achieve $T_H = 185 \pm 7\,^{\circ}C$. Fig. 8a shows the temperature swing ΔT at points A and B as a function of frequency f. It indicates that the temperature swing decreases as the piston frequency increases. This can be attributed to the thermal inertia of the working fluid and of the pyroelectric elements. Indeed, as the piston frequency increases, there is less time for the thermal energy to be exchanged between the heating band or heat exchanger

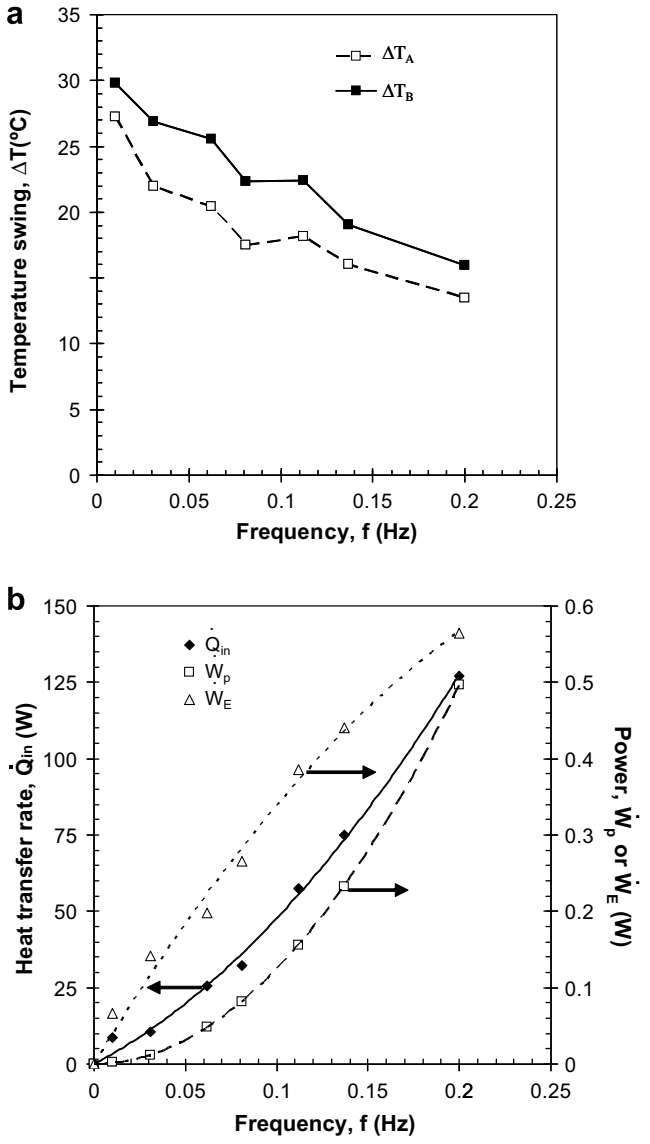

Fig. 8. (a) Temperature swing at points A and B as a function of piston frequency and (b) Heat transfer rate $\dot{Q}_{in}$, pumping power $\dot{W}_p$, and generated electrical power $\dot{W}_E$ as a function of frequency for 50 cst silicone oil as the working fluid and PZST as the pyroelectric elements.

and the fluid and between the fluid and the PEs. This limitation can be addressed by reducing the thermal time constant of the pyroelectric material defined from lump capacitance approximations as $\tau_t = (\rho_{PE}\mathbf{V}_{PE}c_{p,PE})/(h_\omega A)$ [19] where $\mathbf{V}_{PE}$ is the volume of one pyroelectric element.

4.3. Performance analysis

In order to assess the performance of the pyroelectric converter and identify the optimum operating frequency, the average thermodynamic energy efficiency of the system over a cycle is defined as,

$$\eta = \frac{\dot{W}_E}{\dot{Q}_{in} + \dot{W}_p} \tag{19}$$

where $\dot{Q}_{in}$ is the total thermal power provided to the converter, $\dot{W}_E$ is the total electrical power generated, and $\dot{W}_p$ is the pumping power provided by the piston. Note that all other losses such as heat losses to the surrounding and current leakages in the electrical circuit are neglected for the sake of simplicity. Thus, η represents the maximum efficiency achievable by the device. Olsen et al. [12] ignored the pumping power in calculating the efficiency on the basis that it is negligible compared with $\dot{Q}_{in}$. However, it can become significant for high frequencies, small channel widths, and/or more viscous fluids. Then, mass and momentum equations must be solved to compute $\dot{W}_p$.

The total electrical power generated by the two pyroelectric stages in all channels is defined as,

$$\dot{W}_E = Nf\left(\oint V_1 A_1 \, dq_1 + \oint V_2 A_2 \, dq_2\right) \tag{20}$$

where N is the total number of walls with two pyroelectric elements PE_1 and PE_2 at two stages along each channel. The surface areas A_1 and A_2 of each pyroelectric plate are both equal to 9.652 cm^2. The graphical interpretation of the integral $\oint V\,dq$ is illustrated by the area enclosed in gray lines in Fig. 1. A linear interpolation of the charge–voltage curves of temperatures 152, 171, and 194 °C shown in Fig. 1 for PZST [7] is used to determine the hysteresis curve at the computed temperatures T_{cool} and T_{hot} at points A and B (Fig. 2). Due to a lack of experimental data for the charge–voltage curves, PE_1 and PE_2 are assumed to be made of the same material and, therefore, have the same charge–voltage curves shown in Fig. 1 and Curie temperature of $T_{Curie} = 240$ °C. This was not the case experimentally [2]. The electrical power generated by the pyroelectric converter is calculated for V_L and V_H equal to 100 and 700 V, respectively.

Moreover, the total pumping power required to pump the fluid back and forth in the channels is assumed to be only due to frictional losses within the channel. Therefore, the total pumping power over the time period τ (=1/f) is denoted by $\dot{W}_p$ and defined as,

$$\dot{W}_p \approx \frac{(N+1)}{\tau}\int_0^\tau \left(\int_{A_c} p_f v_f dA\right) dt \tag{21}$$

where the local instantaneous fluid velocity v_f and pressure p_f are uniform across the channel width at $z = 0$. Time averaging was performed over a period of oscillation $\tau = 1/f$. The integrals in Eqs. (20) and (21) are computed by using the trapezoidal rule.

Furthermore, the total heat transfer rate provided by the heating band to the converter can be computed as,

$$\dot{Q}_{in} = 2(N+1)q''_{in}A_{hb} \tag{22}$$

where A_{hb} is the surface area of the heating band in one channel equal to 2.413 cm^2.

Fig. 8b shows the heat transfer rate $\dot{Q}_{in}$, the pumping power $\dot{W}_p$, and the generated electrical work $\dot{W}_E$ of the pyroelectric converter as a function of frequency. It indicates that, although the pumping power $\dot{W}_p$ increases rapidly, it is indeed negligible compared with the heat transfer rate $\dot{Q}_{in}$ for the frequencies, channel width, and working fluid considered. Moreover, as seen from the slopes of $\dot{W}_E$, $\dot{W}_p$, and $\dot{Q}_{in}$ in Fig. 8b, the generated electrical power increases less rapidly than the heat transfer rate and pumping power as frequency increases. Note that despite the decrease in temperature swings ΔT_A and ΔT_B (Fig. 8a) the generated power $\dot{W}_E$ increases with frequency.

Finally, Fig. 9 compares the overall thermodynamic efficiency and the ratio of the efficiency η over the Carnot efficiency η_{Carnot} predicted numerically with that measured experimentally by Olsen et al. [2]. The Carnot efficiency η_{Carnot} is defined as,

$$\eta_{Carnot} = 1 - \frac{T_C}{T_H} \tag{23}$$

For the simulated pyroelectric converter, $T_C = 145$ °C (418.15 K), $T_H \approx 185$ °C (458.15 K), and the Carnot efficiency is approximately 8.73%. Fig. 9 shows that there exists a maximum efficiency of 1.33% for frequency $f = 0.031$ Hz representing 16% of the Carnot

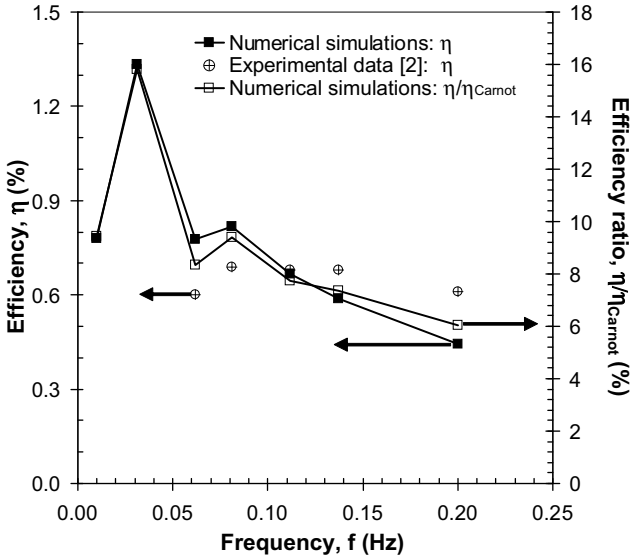

Fig. 9. Efficiency η and efficiency ratio $\eta/\eta_{\text{Carnot}}$ as a function of frequency for the numerical simulation and experimental data [2]. $\eta_{\text{Carnot}} = 8.73\%$.

efficiency. The minimum and maximum relative errors between the numerical predictions and the experimental results are 2% at $f = 0.112$ Hz and 29% at $f = 0.062$ Hz, respectively. Note that these errors can be attributed to (i) the imposed heat transfer rate $\dot{Q}_{\text{in}}$ which can be as low as 50% of that reported by Olsen et al. [2] in order to have $T_{\text{H}} \approx 185\ ^{\circ}\text{C}$, and (ii) the numerical simulations which underpredict the reported generated electrical power $\dot{W}_{\text{E}}$ by as much as 56%. The low $\dot{Q}_{\text{in}}$ imposed can be attributed to experimental heat losses to the surrounding/air and to experimental thermal losses caused by parts of the heating band located outside the working fluid. These experimental considerations were ignored in the present numerical study. The error on $\dot{W}_{\text{E}}$ is due to the following approximations: (1) the pyroelectric material considered had different material properties, Curie temperature, and q–V curves from those used experimentally, (2) all charge–voltage curves were linearly interpolated between the three experimentally measured nonlinear charge–voltage curves [7], and (3) the pyroelectric elements PE_1 and PE_2 were assumed to be identical. In general, the data agrees relatively well with the experimental data [2] and is found acceptable based on the assumptions made and the available material properties.

4.4. Optimum performance

The power density of the pyroelectric converter represents the total amount of electrical power generated per unit volume of pyroelectric elements. It is defined as,

$$P_{\text{D}} = \frac{\dot{W}_{\text{E}}}{2(N+1)V_{\text{PE}}} \tag{24}$$

Eqs. (4) and (5) suggest that the product ρc_p is a parameter affecting the temperature swing of both the working fluid and the wall. In turn, it affects both the overall thermodynamic efficiency η and the power density P_{D} of the pyroelectric converter. Thus, the following cases are investigated to determine the effects of ρc_p of the working fluid and/or pyroelectric material on the efficiency and power density of the pyroelectric converter:

1. Case 1 is the baseline case discussed previously using properties given in Table 1.
2. Case 2 uses the same properties as Case 1 except for $\rho_{\text{PE}} c_{p,\text{PE}}$ which is divided by a factor of 2.
3. Case 3 uses the same properties as Case 1 except for $\rho_{\text{PE}} c_{p,\text{PE}}$ which is divided by a factor of 4.
4. Case 4 uses the same properties as Case 1 except for $\rho c_{p,\text{PE}}$ of both the pyroelectric element and the working fluid which are both divided by a factor of 2.
5. Case 5 uses the same properties as Case 1 except for $\rho_{PE} c_{p,PE}$ and $\rho_{\text{f}} c_{p,f}$ which are divided and multiplied, respectively, by a factor of 2.

Fig. 10 shows the efficiency η and the efficiency ratio $\eta/\eta_{\text{Carnot}}$ as a function of frequency for Cases 1 through 5. It indicates that the efficiency increases as ρc_p of the pyroelectric element and/or the working fluid decreases. The optimum frequency occurs below 1 Hz for all cases. The increase in efficiency can be attributed to the fact that the thermal time constant of the pyroelectric element τ_t decreases in Cases 2 and 3 and that the heat transfer rate required to maintain the heating band at $T_{\text{H}} = 185\ ^{\circ}\text{C}$ decreases as

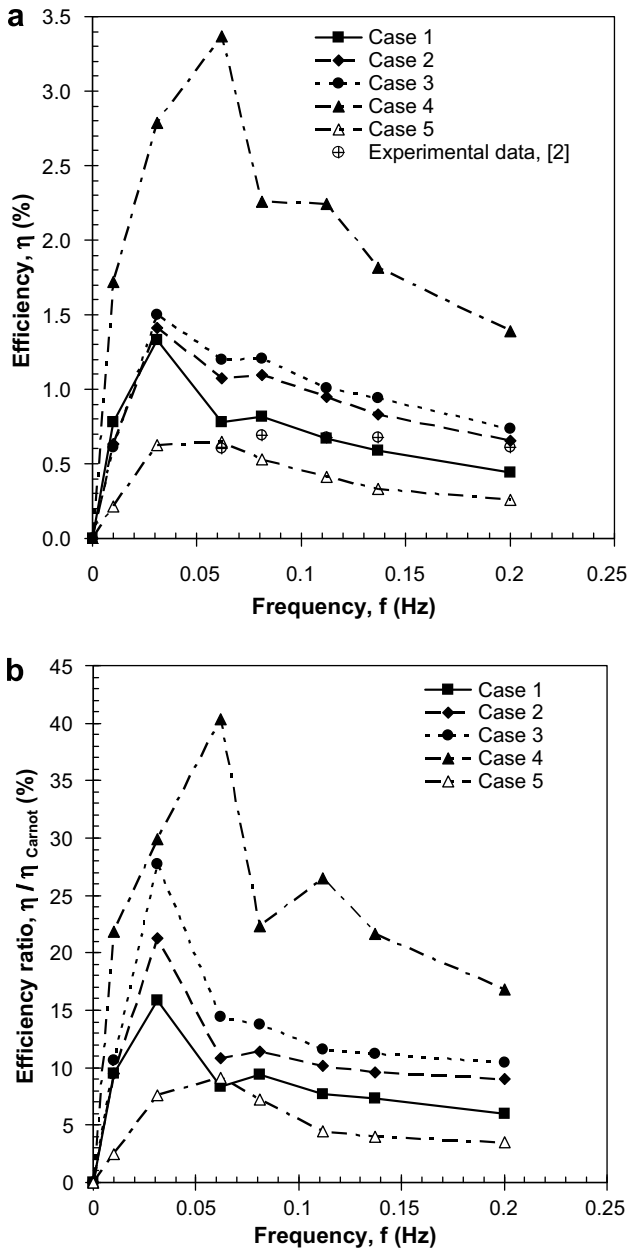

Fig. 10. (a) Efficiency η as a function of frequency and (b) efficiency ratio $\eta/\eta_{\text{Carnot}}$ as a function of frequency for Cases 1 through 5. $\eta_{\text{Carnot}} = 8.73\%$.

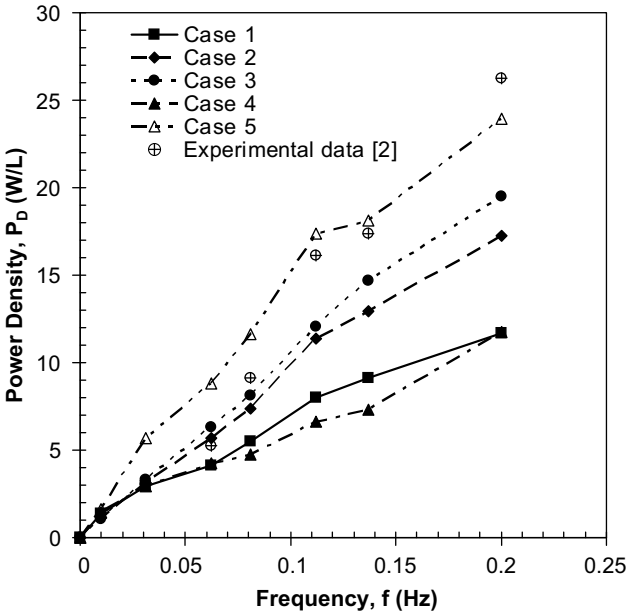

Fig. 11. Power density as a function of frequency for the numerical simulation and experimental data [2].

ρc_p of the fluid decreases in Case 4. Fig. 10 suggests that a maximum efficiency of 3.4% can be achieved at $f = 0.062$ Hz for Case 4, or 40% of the Carnot efficiency.

Fig. 11 shows the power density P_D as a function of frequency for Cases 1 through 5 as well as those measured experimentally [2]. For all simulations, the power density increases as frequency f increases since $\dot{W}_E$ is proportional to f. In addition, Fig. 11 shows that, for a given frequency, P_D increases as ρc_p of the pyroelectric material decreases. Indeed, as the working fluid exchanges a certain amount of energy with the PE, the PE temperature swing is larger for smaller ρc_p. On the other hand and unlike the efficiency, P_D increases as ρc_p of the working fluid increases. Indeed, larger values of ρc_p enable the working fluid to stored more thermal energy as it passes by the heating element and later deposit it into the PEs. This results in an increase in the PEs' temperature swing and in $\dot{W}_E$. Fig. 11 suggests that a power density of 24 W/L of PZST can be achieved at $f = 0.2$ Hz for Case 5. Practically, the desired value of ρc_p of the working fluid could be achieved by using nanofluids. In addition, the use of nanofluids could possibly enhance the convective heat transfer [23] between the fluid and the PEs as well as the heat and cold sources.

5. Conclusion

This study was concerned with numerical simulations of a prototypical pyroelectric converter assembled by Olsen et al. [2]. It established that

1. the mass, momentum, and energy equations must be solved simultaneously in order to compute the pumping power and accurately predict the temperature oscillations of the PEs,
2. the velocity profile is fully developed at all times when the fluid reaches the active region of the converter,
3. the temperature is uniform across the pyroelectric element,
4. the pumping power is negligible compared with the heat transfer rate for the frequency range, channel width, and working fluid considered,
5. the pyroelectric converter operates less efficiently at frequencies greater than 1 Hz because the heat transfer rate increases more rapidly than the generated electrical power as frequency is increased,
6. the important parameters in the pyroelectric converter are the frequency of oscillation and ρc_p of both the working fluid and the pyroelectric material,
7. the efficiency of the pyroelectric converter increases with smaller values of ρc_p of the working fluid and of the pyroelectric material and operates most efficiently at a frequency less than 1 Hz, and
8. the power density of the pyroelectric converter increases with larger frequencies, smaller values of ρc_p of the pyroelectric material, and larger values of ρc_p of the working fluid.

Future work should account for temperature dependent properties and use experimentally determined charge–voltage curves of the PEs at different temperatures in order to accurately predict the electrical work generated and the overall thermodynamic efficiency.

Acknowledgements

This work was funded in part by the Office of Naval Research under Award N000140710671 (Program manager: Dr. Mark Spector). The authors would like to thank Dr. R. Olsen for useful discussions and exchange of information.

References

[1] S. Riffat, X. Ma, Thermoelectrics: a review of present and potential applications, Appl. Therm. Eng. 23 (2003) 913–935.
[2] R. Olsen, D. Bruno, J. Briscoe, Cascaded pyroelectric energy converter, Ferroelectrics 59 (1984) 205–219.
[3] R. Olsen, D. Bruno, J. Briscoe, Pyroelectric conversion cycles, J. Appl. Phys. 58 (1985) 4709–4716.
[4] R. Olsen, D. Bruno, J. Briscoe, W. Butler, A pyroelectric energy converter which employs regeneration, Ferroelectrics 38 (1981) 975–978.
[5] R. Olsen, Ferroelectric conversion of heat to electrical energy – a demonstration, J. Energy 6 (1982) 91–95.
[6] R. Olsen, D. Brown, High-efficiency direct conversion of heat to electrical energy related pyroelectric measurements, Ferroelectrics 40 (1982) 17–27.
[7] R. Olsen, D. Bruno, J. Briscoe, Pyroelectric conversion cycle of vinylidene fluoride–trifluoroethylene copolymer, J. Appl. Phys. 57 (1985) 5036–5042.
[8] M. Ikura, Conversion of low-grade heat to electricity using pyroelectric copolymer, Ferroelectrics 267 (2002) 403–408.
[9] L. Kouchachvili, M. Ikura, High performance pyroelectric converter, in: Proceedings of the Sixth IASTED International Conference European Power and Energy Systems, Rhodes, Greece, 2006, pp. 366–371.
[10] S. Lang, Pyroelectricity: from ancient curiosity to modern imaging tool, Phys. Today 58 (2005) 31–36.
[11] J. Zemel, Future directions for thermal information sensors, Sensors Actuat. A 56 (1996) 57–62.
[12] R. Olsen, W. Butler, J. Drummond, D. Bruno, J. Briscoe, Heat flow in a pyroelectric converter, in: Proceedings of the 20th Intersociety Energy Conservation Engineering Conference, Miami Beach, FL, vol. 3, 1985, pp. 595–602.
[13] E. Fatuzzo, H. Kiess, R. Nitsche, Theoretical efficiency of pyroelectric power converters, J. Appl. Phys. 37 (1966) 510–516.
[14] A. van der Ziel, Solar power generation with the pyroelectric effect, J. Appl. Phys. 45 (1974) 4128.
[15] R. Olsen, D. Evans, Pyroelectric energy conversion: hysteresis loss and temperature sensitivity of a ferroelectric material, J. Appl. Phys. 54 (1983) 5941–5944.
[16] P. Bouvier, P. Stouffs, J. Bardon, Experimental study of heat transfer in oscillating flow, Int. J. Heat Mass Transfer 48 (2005) 2473–2482.
[17] A. Bejan, Convection Heat Transfer, third ed., Wiley, New York, 2004. p. 2, 7, 15.
[18] D.C. Corp., Dow corning 200(R) fluid, 50 cst (March 28, 2007). <www.dowcorning.com/applications/search/default.aspx?R=75EN>.
[19] F. Incropera, D. DeWitt, Heat and Mass Transfer, fourth ed., Wiley, New York, 2002. pp. 242, 436–438, 823.
[20] L. Shin-Etsu Chemical Co., Products (March 28, 2007). <www.silicone.jp/e/products/oil/about/feature.html>.
[21] P. Ceramic, Piezoceramic materials (March 28, 2007). <www.piceramic.de/pdf/piezo-material.pdf>.
[22] H. Atabek, C. Chang, Oscillatory flow near the entry of a circular tube, Z. Angew. Math. Phys. 12 (1961) 185–201.
[23] Y. He, Y. Jin, H. Chen, Y. Ding, D. Cang, H. Lu, Heat transfer and flow behaviour of aqueous suspensions of TiO_2 nanoparticles (nanofluids) flowing upward through a vertical pipe, Int. J. Heat Mass Transfer 50 (2007) 2272–2281.